

Research Article

Failure Modes and Resistance of Perforated Steel Rib Shear Connectors under Uplift Forces

Xiaoqing Xu ^{1,2} and Yuqing Liu ³

¹Ph.D. Lecturer, School of Civil Engineering, Chongqing University, Chongqing 400045, China

²Key Laboratory of New Technology for Construction of Cities in Mountain Area (Ministry of Education), Chongqing University, Chongqing 400045, China

³Ph.D. Professor, Department of Bridge Engineering, Tongji University, Shanghai 200092, China

Correspondence should be addressed to Yuqing Liu; yql@tongji.edu.cn

Received 9 September 2018; Revised 10 December 2018; Accepted 10 January 2019; Published 6 March 2019

Academic Editor: Flora Faleschini

Copyright © 2019 Xiaoqing Xu and Yuqing Liu. This is an open access article distributed under the Creative Commons Attribution License, which permits unrestricted use, distribution, and reproduction in any medium, provided the original work is properly cited.

In recent years, there is a rapid increase in the application of perforated steel rib shear connectors in steel and concrete composite structures. The connectors must not only ensure shear transfer but also sufficient uplift resistance. The shear behavior of connectors has been extensively investigated. However, studies on uplift resistance are lacking so far. Therefore, three push-out test specimens were tested to investigate the shear and tension behavior of perforated L-shaped and plain steel rib shear connectors. The failure modes of connectors were analyzed, and analytical models for the determination of uplift resistance were derived based on test results. The results showed that the ductility of perforated steel rib shear connectors under uplift force was smaller than that under shear force, and more severe concrete damage surrounding the rib and larger bending deformation of transverse steel bar was observed. The rib flange of L-shaped perforated rib has a significant contribution to the uplift resistance. It was suggested to increase the rib height of L-shaped rib to avoid the horizontal crack at the height of the rib flange. The validity of the proposed analytical models was confirmed by comparing the failure modes and capacities of specimens.

1. Introduction

In steel and concrete composite structures, various types of shear connectors, such as headed stud shear connector [1] and perforated steel rib shear connector [2], are arranged to ensure the composite action between the steel and concrete components. A perforated steel rib shear connector is a thin steel plate with a number of uniformly spaced holes. After the holes in the perforated rib are filled with concrete, the concrete dowel can resist longitudinal shear and prevent uplift separation between steel and concrete components [2–5]. Though the headed stud shear connector is still the most widely used shear connector, there is an increase in applications of perforated steel rib shear connectors in the composite structures [5–9], owing to their ease of manufacture, excellent load bearing and deformation properties, superior antifatigue performance, and usefulness in slender concrete slabs [10].

In the literature, the shear behavior of perforated steel rib shear connectors has been studied extensively [4, 11, 12] since the earlier research work of Leonhardt et al. [2], and several formulas for estimating the shear resistance of perforated steel rib shear connectors have been proposed for the shear design of the connectors in composite structures. The research studies on perforated steel rib shear connectors have shown that the shear behavior is significantly influenced by a number of parameters, including the hole diameter, the number of holes, the compressive strength of concrete, the thickness, length and height of the steel plate, the configuration of transverse steel bar in the hole, and the dimension of concrete slab [4]. Besides the traditional perforated steel rib with closed recesses, rib connectors with open recesses have developed in recent times. For the rib connectors with open puzzle-shaped geometry, intense research for the assessment of the shear behavior of rib shear connectors

was performed in [13, 14] for steel failure, in [15–17] for concrete failure, and in [18] for fatigue failure. These experimental and theoretical studies led to the development of design principles for puzzle-shaped rib shear connectors under shear forces.

With the increase of composite structures and the widespread use of perforated steel rib shear connectors, it is becoming more common for connectors to be subjected to uplift forces. The behavior of composite structures would be significantly affected by the performance of perforated steel rib shear connectors under uplift forces. As shown in Figure 1(a), the connectors in steel-concrete composite beams exposed to bending should provide sufficient resistance against the uplift of the concrete slab. In composite slabs, the perforated steel rib shear connector is subjected to both the shear and uplift forces, especially when the shear crack occurs in the slab and results in vertical relative slip between steel ribs and concrete, as shown in Figure 1(b). In integral steel bridges, perforated steel rib shear connectors were reported to be installed at the end diaphragm of the steel girder to improve load- and crack-resisting capacity of the girder-abutment joints (Figure 1(c)) [19]. In Figure 1(d), the out-plane deformation of steel tube in concrete-filled steel tubular columns could be restrained by perforated steel rib shear connectors which thus were in tension [20]. In such composite structures, the perforated steel rib shear connectors must not only ensure shear transfer but also sufficient uplift resistance. According to the design provisions for composite beams in Eurocode 4 [21], shear connectors should be designed to resist a nominal ultimate tensile force, perpendicular to the plane of the steel flange, of at least 0.1 times the design ultimate shear resistance of the connectors. While headed stud shear connectors are generally assumed to provide sufficient resistance to uplift [21], there are no official guidelines for the design of the uplift resistance of rib shear connectors in the codes. Only few tests on puzzle-shaped rib shear connectors with open recesses were carried out to investigate the resistance of rib shear connectors under tension [22–25] or combined shear and tension [26, 27]. However, studies on rib shear connectors with closed recesses (traditional perforated steel rib) are lacking so far. Therefore, the focus in this study is on the behavior of perforated steel rib shear connectors subjected to uplift forces.

The perforated steel ribs can act as not only shear connectors but also stiffeners for the steel plate in composite slabs. The perforated L-shaped ribs proposed by Xu et al. [5] and used in composite slabs, as shown in Figure 2, have been proved to reduce the shear crack risk of composite bridge deck slabs and have a larger contribution to the loading-carrying capacities of composite slabs than plain ribs. However, it is still not clear that how perforated ribs resist the vertical relative slip between steel ribs and concrete after the shear crack occurred. In this study, perforated L-shaped and plain steel rib shear connectors were tested under uplift forces. The failure modes of two types of rib shear connectors were analyzed, and analytical models for the determination of the uplift resistance were derived based on test results.

2. Push-Out Tests

To investigate the structural behavior of perforated steel rib shear connectors, three push-out test specimens were fabricated and tested with no redundancy, among which two specimens reflecting the real state of perforated rib in composite slabs were designed and tested for the uplift resistance. The failure modes and load-slip curves of the specimens are reported.

2.1. Test Programs. Table 1 summarizes the geometric properties of the specimens together with the properties of materials used in this study. d and d_s are, respectively, the diameter of the hole and steel bar in the hole, and the yield strength of the bar ($f_{y,bar}$) is 450 MPa. The yield strength of the steel rib ($f_{y,rib}$) is 365 MPa. The concrete cubic and cylinder compressive strength (f_{cu} and f'_c), tensile strength (f_{ct}), and modulus of elasticity (E_c) on the day of the test are presented.

The specimens were designed based on the design of the composite slabs reported in [5]. Their details are shown in Figure 3. The photos of steel members of the specimens are shown in Figure 4. S-1 specimen is a traditional push-out test specimen. Two steel plate of 6 mm thickness, 350 mm height, and 100 mm width were welded in vertical direction to a steel plate of 20 mm thickness. The thicker steel plate was subjected to a vertical load which produces a shear load along the interface between the concrete slab and steel member. At the end of the steel plate, plastic foam blocks were set to eliminate the end-bearing effect of concrete. T-1 and T-2 specimens were designed to study the uplift behavior of the perforated rib in steel and concrete composite slabs. One steel plate of 6 mm thickness, 100 mm height, and 180 mm width was welded in horizontal direction to a steel plate of 20 mm thickness. Through two vertical steel plates, vertical loads were applied symmetrically to two ends of the horizontal steel plate. S-1 and T-1 specimens were fabricated with plain steel ribs, while L-shaped steel rib was used in T-2 specimen. The width of the L-shaped steel rib flange was 30 mm, as shown in Figure 3(c). All steel members were cast into concrete block with a thickness of 150 mm which is the same with that of the bridge deck slab reported by Xu et al. [5]. Referring to Figure 5, in all the specimens, transverse steel bars of 14 mm diameter were placed through the center of the holes. Reinforcing bars of 10 mm diameter were arranged above the steel ribs with a spacing of 100 mm. Additional rebars were placed under the transverse bars in T-type specimens to avoid the premature bending failure of specimens. These rebars were placed more than 100 mm away from the ribs in order to minimize their effects on the failure modes of the connectors.

As shown in Figure 6, the test setup is similar to that used in earlier push-out tests [4]. Load was applied using a hydraulic testing machine of 2000 kN capacity. The loading procedure is shown in Figure 7. P_u is the estimated ultimate load, which was obtained through preliminary calculation before the tests. It was initially taken as 380 kN, and then it was adjusted to 360 kN after the test of S-1 specimen. After

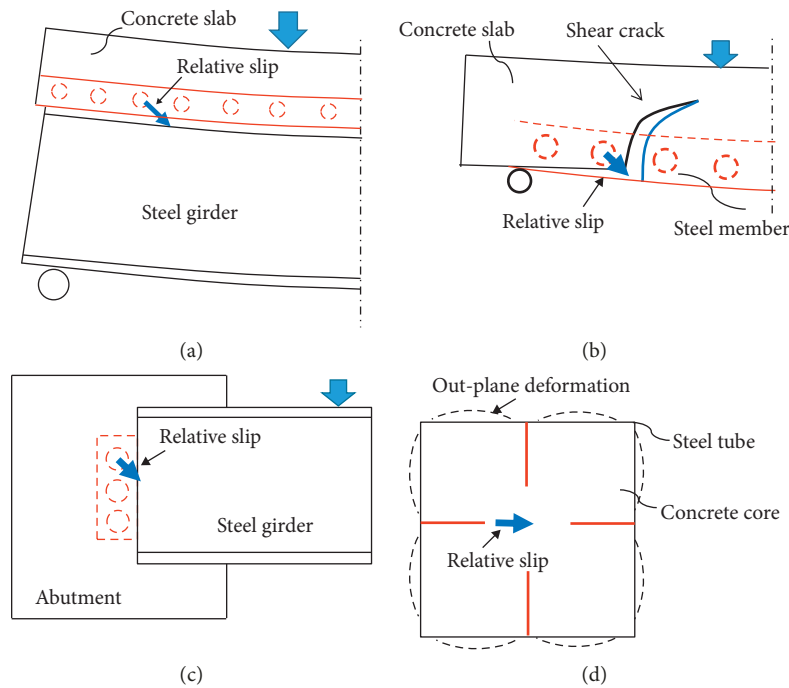


FIGURE 1: Perforated steel rib shear connectors subjected to uplift forces. (a) Composite beam. (b) Composite slab. (c) Girder-abutment joint. (d) Concrete-filled steel tubular column.

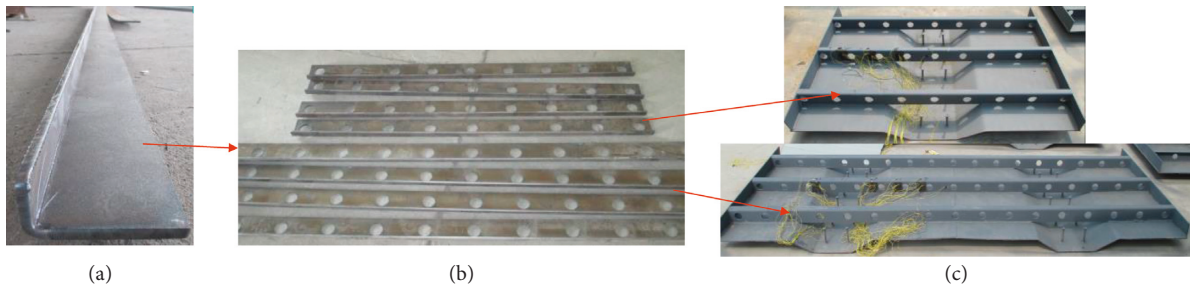


FIGURE 2: Application of perforated L-shaped steel ribs in composite slabs [5]. (a) L-shaped steel rib. (b) Perforated L-shaped steel ribs. (c) Steel members of steel and concrete composite slabs.

TABLE 1: Specimen characteristics and material properties.

Label	Force	Rib type	Number of holes	d (mm)	d_s (mm)	$f_{y,rib}$ (MPa)	$f_{y,bar}$ (MPa)	f_{cu} (MPa)	f'_c (MPa)	f_c (MPa)	E_c (MPa)
S-1	Shear	Plain	2								
T-1	Uplift	Plain	1	50	14	365	450	51.8	43.0	4.6	40600
T-2	Uplift	L-shaped	1								

preloading, five low level and five high level load cycles were applied before the specimens were loaded to failure or the slip up to 20 cm. The loading speed was controlled under 30 kN/min or 1 mm/min.

Figure 8 presents the arrangement of the measuring system. D1 to D4 are displacement transducers (LVDTs) to measure the vertical relative slip between the concrete slab and the steel member. Strain gauges (G1 to G8) were attached to the steel members and bars. In this figure, the long side of the black rectangle representing the strain gauge is the direction of the strain gauge. Data were acquired using a

personal computer-based data acquisition system and were continuously sampled at a rate of 1 Hz during the test.

2.2. Failure Modes. The failure of S-1 specimen was triggered by the longitudinal splitting of the concrete slab, followed by the crushing of concrete on the bottom of the specimen as shown in Figure 9(a). The concrete cracks were firstly observed at the load of about 570 kN, and then they propagated and the crack width increased with the increase of the load and the number of the load cycles.

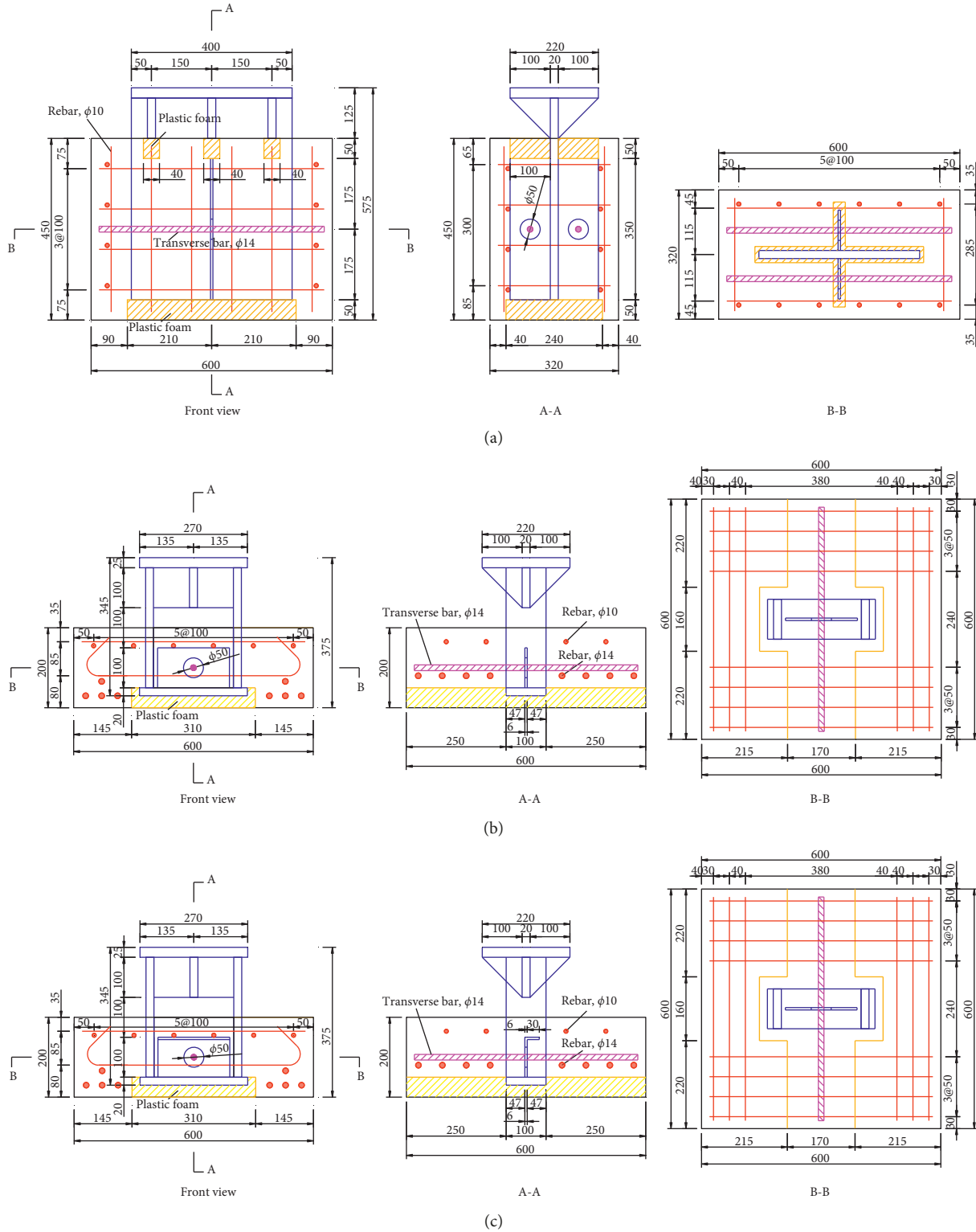


FIGURE 3: Details of the specimens (mm). (a) S-1. (b) T-1. (c) T-2.

Two T-type specimens exhibited similar failure modes. Approaching the ultimate load, at the bottom surface of the concrete block, transverse concrete cracks were observed on both sides in Figure 9. At the end of the test, concrete

cones with a height of about 5 cm between the two transverse cracks were punched out along with the steel member. In Figure 10, the sectional views through both test specimens show the punching cracks and concrete cones



FIGURE 4: Photos of steel members. (a) S-1. (b) T-1. (c) T-2.

clearly. In the T-2 specimen with L-shaped rib, horizontal cracks were initiated near the short leg of L-shaped rib while during the test of T-1 specimen, no crack was observed.

The concrete slabs were opened after the experiment. Considerable bending and shear deformation of the transverse steel bars were observed, as shown in Figure 11. At the locations of perforation, the deformation of steel bars was the largest, which resulted in V-shaped bars. The bar in T-1 specimen was deformed almost symmetrically, while in T-2 specimen, the right part of the bar, which was at the same side with the short leg of L-shaped rib, had smaller bending deformation.

As shown in Figure 12, local plastic deformation occurred on the top edge of the holes in T-1 and T-2

specimens. Meanwhile, in T-2 specimen, the rib flange bent up visibly under the pressure from the concrete below.

2.3. Load-Relative Slip Curves and Load Capacities. Figure 13 shows the load-relative slip curves. It is noted that for S-1 specimen, the load for one rib connector is the half of the applied load in the test. At the early stage of loading, there was almost no relative slip between the steel plate and the concrete block. The shear force was mainly carried by the initial interface bond. Then, with the initiation and development of the relative slip, the interface bond was failed and the bond stress gradually reduced. At the same time, the dowels through the holes in the ribs started to resist the increasing external force. S-1 specimen presents the largest

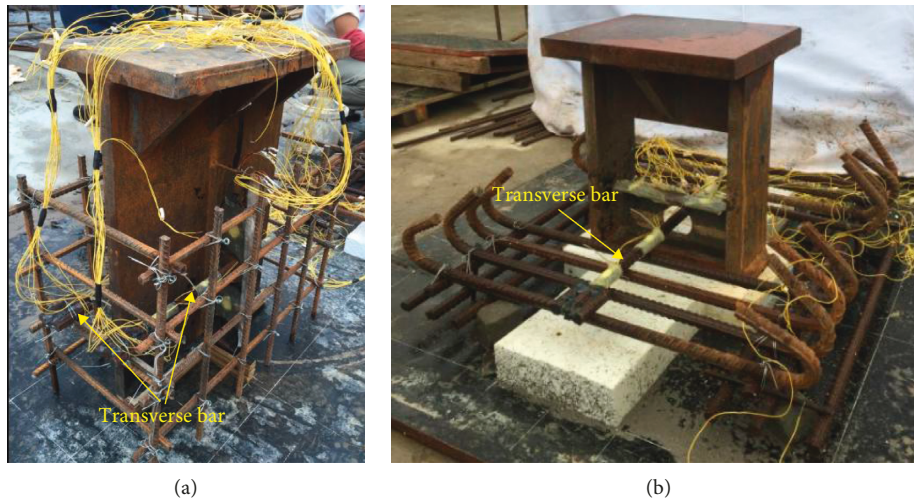


FIGURE 5: Photos of steel bar arrangement. (a) S-1. (b) T-type specimen.

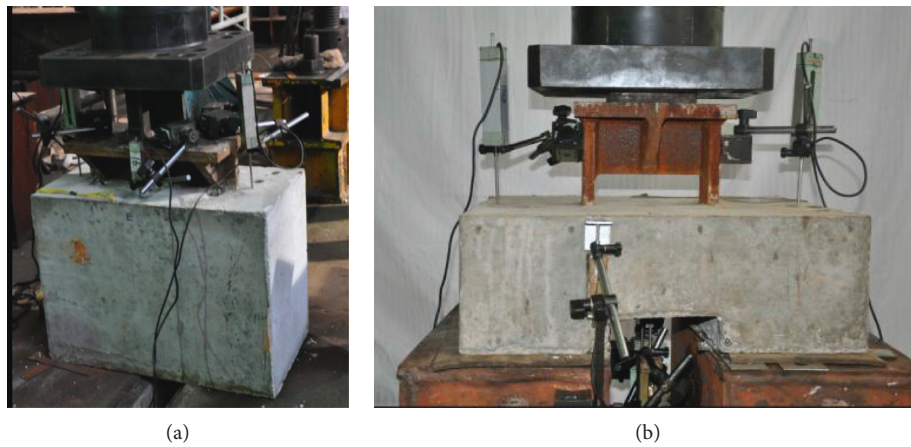


FIGURE 6: Test setup. (a) S-1. (b) T-type specimen.

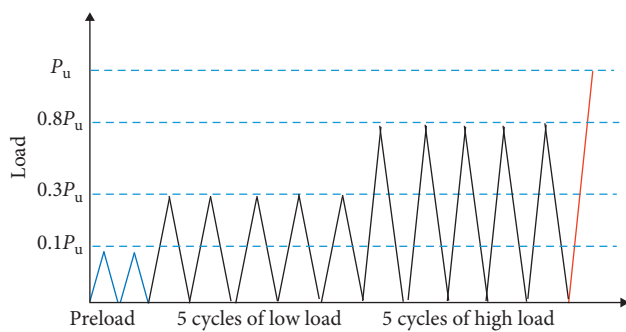


FIGURE 7: Push-out test loading sequence.

ductility. After reaching the peak point, the load in T-type specimens decreased rapidly while in S-1 specimen, the load gradually dropped only by 10%.

Table 2 summarizes the residual load capacity F_r , the ultimate load F_u , and the relative ultimate slip S_u . F_r is defined as the load value at the relative slip of 15 mm. F_r of S-1 specimen is more than 2 times as large as those of T-type specimens. T-1 specimen has an ultimate strength 12.0%

larger than that of T-2 specimen. S_u of S-1 specimen is also the largest. It indicates that when the perforated rib is subjected to uplift force, the capacity and ductility are smaller than those under shear force.

2.4. Strain in Steel Members and Transverse Steel Bars. In Figure 14, the results of vertical strain gauges located 100 mm above or below the rib hole in S-1 specimen were plotted with the relative slip. The value of the strain gauge above the hole was negative and increased with the relative slip. It indicates that the upper part of the rib was in compression. The compressive stress was applied to the rib through the upper part of the rib hole by concrete. The value of the strain gauge below the hole was also negative when the slip was smaller than 0.1 mm. It then became a positive value at the slip of about 0.6 mm. The reversal in the sign of strain was thought to occur when the natural bond between concrete and steel rib failed. The large differences between two strain gauges implied that the shear force had been transferred to concrete through the rib hole.

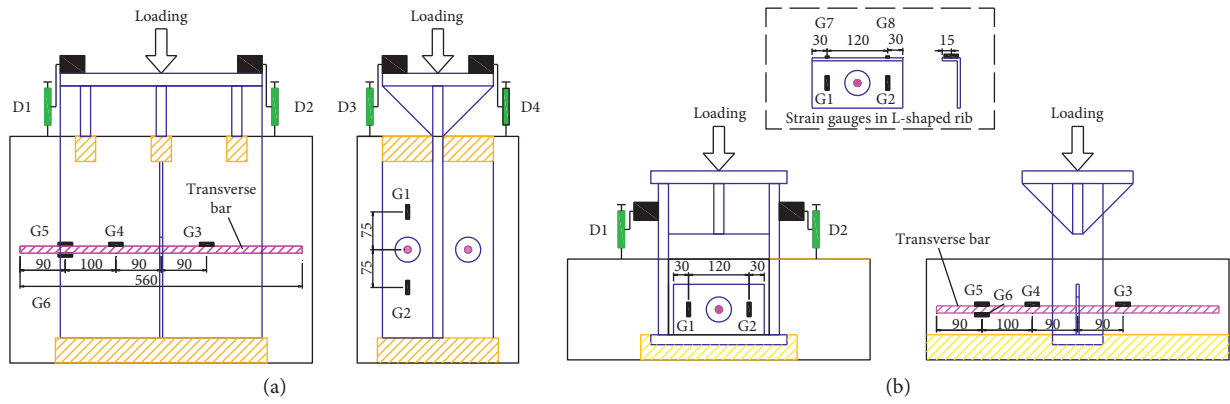


FIGURE 8: Layout of the measurements (mm). (a) S-1. (b) T-type specimen.

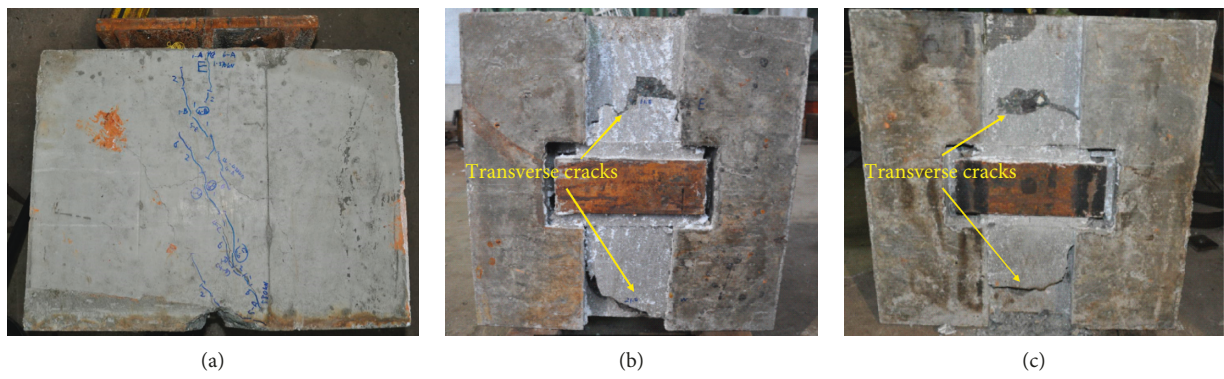


FIGURE 9: Failure modes of specimens. (a) S-1. (b) T-1. (c) T-2.

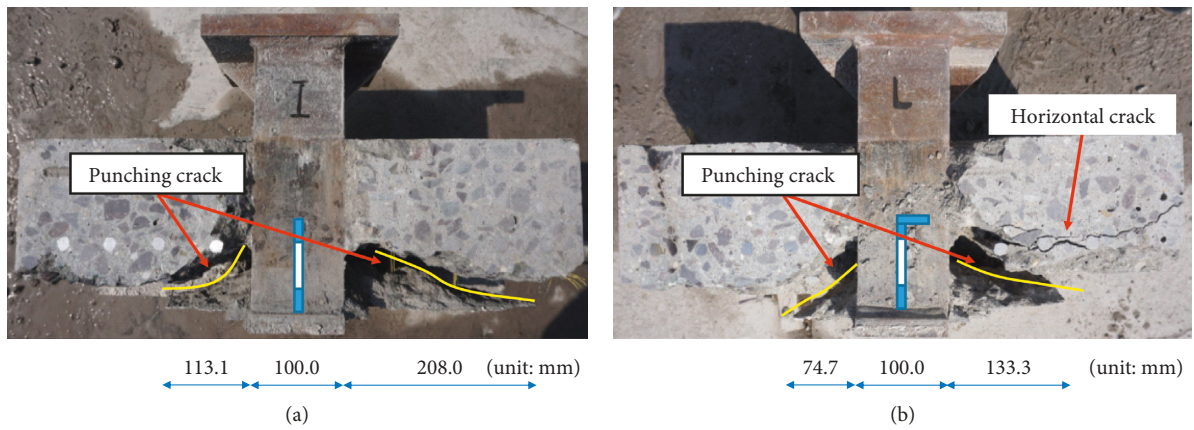


FIGURE 10: Cracks in T-type specimens. (a) T-1. (b) T-2.



FIGURE 11: Deformation states of transverse steel bars. (a) T-1. (b) T-2.

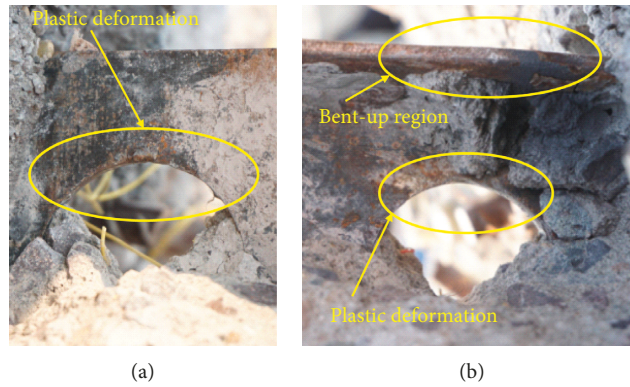


FIGURE 12: Plastic deformation of the steel ribs. (a) T-1. (b) T-2.

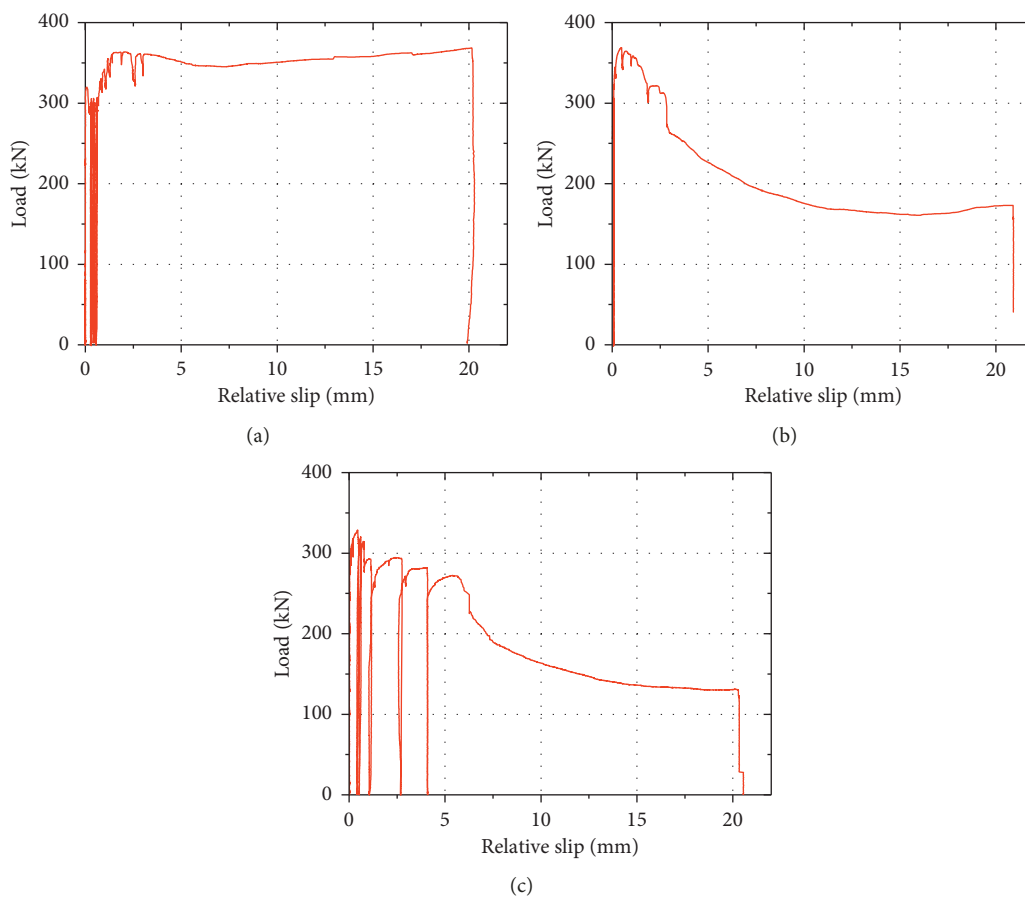


FIGURE 13: Load-slip curves. (a) S-1. (b) T-1. (c) T-2.

TABLE 2: Experimental results.

Label	Force	F_r (kN)	F_u (kN)	S_u (mm)
S-1	Shear	358.0	363.3	2.15
T-1	Uplift	162.0	367.8	0.43
T-2	Uplift	136.2	328.5	0.44

The results of vertical strain gauges near the rib holes in T-1 and T-2 specimens are shown in Figure 15. It was found that the tensile strain in the rib slightly increased at low level

of load when the natural bond between concrete and steel rib mainly resisted the uplift forces, while after the natural bond failed, the strain gradually increased with the load. According to these results, the initial slip loads were evaluated to be 178 kN and 130 kN for T-1 and T-2 specimens, respectively.

Figure 16 shows the horizontal strain in the flange of the steel rib in T-2 specimen. The upside face of the flange was in tension when the load was larger than the initial bond load. When the rib flange was pulled down by the rib web, its deformation was resisted by the surrounding concrete and it would be in bending and tension. The flexural deformation

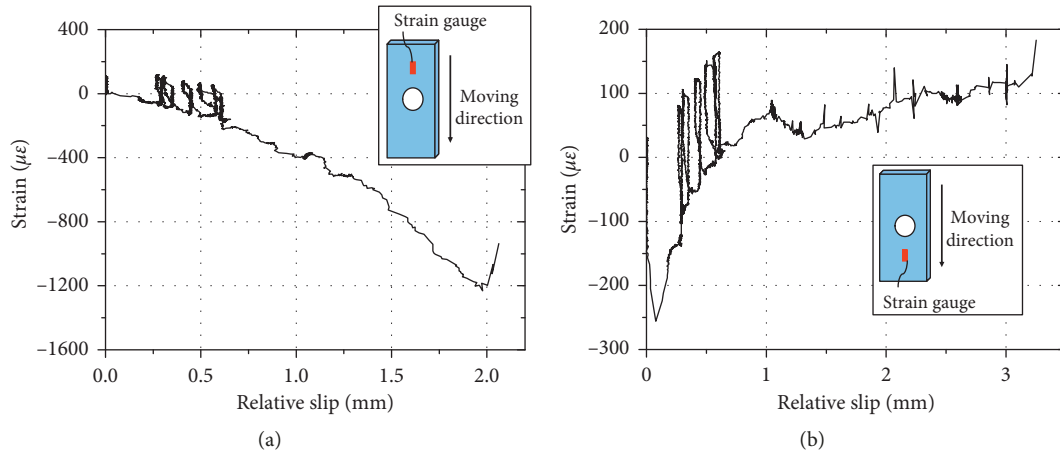


FIGURE 14: Results of vertical strain gauges above or below the rib hole in S-1 specimen. (a) Above the hole. (b) Below the hole.

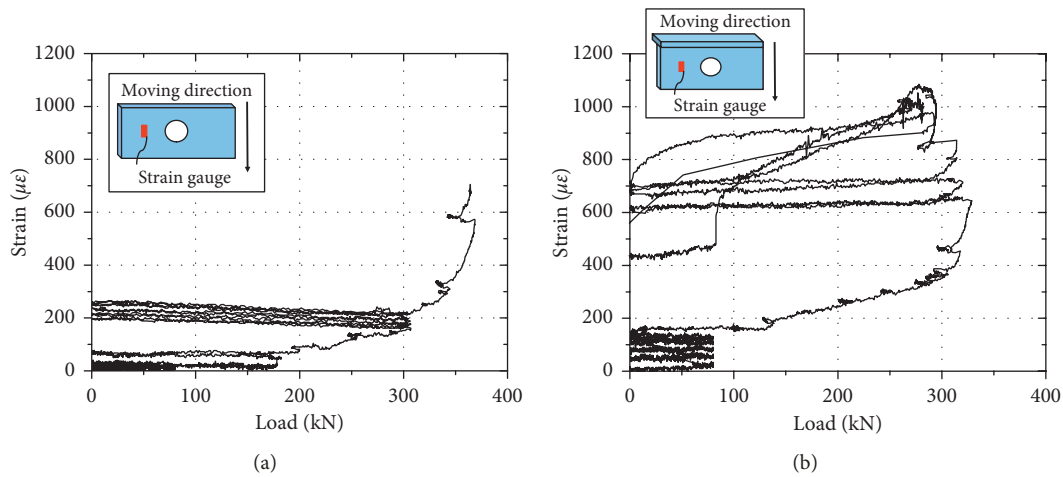


FIGURE 15: Results of vertical strain gauges near the rib holes in T-type specimens. (a) T-1. (b) T-2.

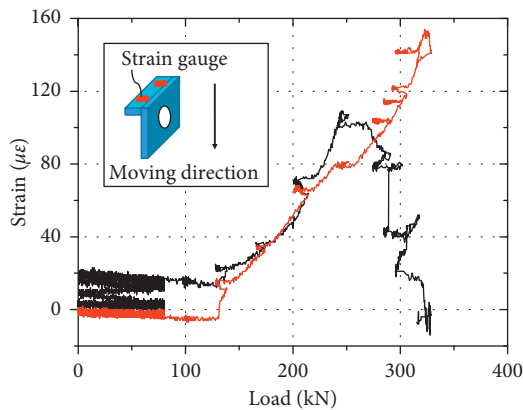


FIGURE 16: Results of horizontal strain gauges on the flange of the L-shaped rib.

of the rib flange, which was also observed in Figure 12, implied that the rib flange has a significant contribution to the uplift resistance of the L-shaped shear connector.

When perforated ribs transfer the longitudinal and vertical shear forces between steel and concrete members, the transverse bars will deform with the concrete around the holes, according to Zheng et al. [4]. The deformation of transverse bars can be taken as an indication of shear forces transferred by perforated ribs. Figures 17 and 18 show the results of strain gauges in the transverse bars in S-1 specimen. It can be seen that the transverse bar was in tension. No. 3 strain gauge is closer to the rib hole, and larger tensile strain was observed. It can be concluded that the tensile force and bending moment decreased along the bar from the rib hole to the bar end. The force exerted to the bar by the concrete in the hole was balanced by the bearing force and bond stress from the concrete around the bar.

The results of no. 3 strain gauges in T-1 and T-2 specimens are shown in Figure 18. The values of strain in transverse bars in these two specimens were more than 4 times larger than that in S-1 specimen. The transverse bars almost or already yielded at a slip smaller than 3 mm, which indicates that the transverse bars in T-1 and T-2 specimens

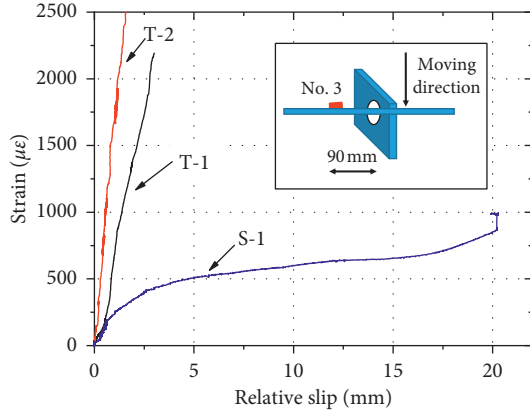


FIGURE 17: Results of no. 3 strain gauges in transverse bars.

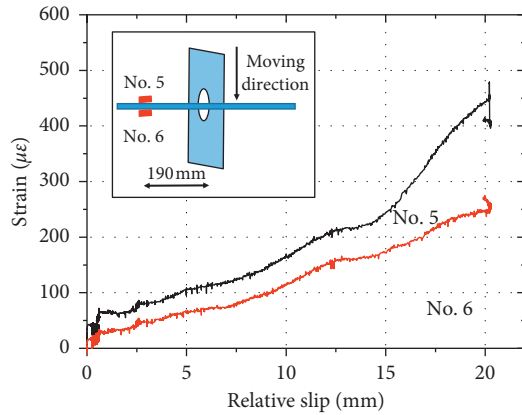


FIGURE 18: Results of no. 5 and no. 6 strain gauges in transverse bar of S-1 specimen.

had larger bending deformation than those in S-1 specimen. The possible reason is that the concrete layer below the transverse bar is thicker in S-1 specimen and thus its constraint on the overall bending deformation of the bar is stronger.

In Figure 19, results of no. 5 and no. 6 strain gauges in transverse bars in T-type specimens are presented. It was found that the bars were in tension and the tensile forces increased with the relative slip, which was also reported in [26, 27]. Compared with the results of strain gauges at the same position in S-1 specimen, it is clear that the bars in T-type specimens have larger deformation.

3. Analytical Models for Predicting Uplift Resistance

The uplift resistance of rib connectors is affected by the performance of concrete, steel rib, and steel bar. In Figure 20, the steel rib, concrete, and bar in the rib hole are detached from the specimen, and the reactions that the remaining concrete and steel bar exert on this free body are shown. The tensile force in the web of steel rib is in vertical equilibrium with four forces: the shear force in the steel rib (F_{hs}), the shear force in the concrete (F_{hc}), the bond and friction in the

interface between concrete and steel rib (F_b), and the vertical force applied to the flange of the L-shaped rib (F_f). These forces are all the resultant of the stresses at the shear connector surface. The equilibrium equation is written as follows:

$$\begin{aligned} F &= F_w = F_h + F_b + F_f, \\ F_h &= F_{hs} + F_{hc}. \end{aligned} \quad (1)$$

3.1. Tensile Strength of Steel Rib Web. The tensile failure of the steel rib web under F_w is ductile. The strength of the web can be evaluated by the following equation:

$$F_{w,u} = f_{y,rib} A_w = f_{y,rib} a_{rib} t_{rib}, \quad (2)$$

where $f_{y,rib}$ is the yield strength of the steel rib and A_w is the cross-sectional area of the web of steel rib. For T-type specimens with steel ribs of 180 mm width (a_{rib}) and 6 mm thickness (t_{rib}), the tensile strength was calculated to be 394.2 kN.

3.2. Resistance of Concrete Dowel and Transverse Steel Bar. Studies on perforated rib shear connectors under shear load have shown that the shear capacity of the connector is mainly contributed by the concrete dowel, chemical bond, and the bar in the hole, and the slip at the ultimate load is generally larger than 1 mm [12].

In this study, equation (3) proposed by Zheng et al. [4] is adopted to estimate the shear capacity of the perforated shear connector:

$$F_{h,u} = 1.76\alpha_A (A_h - A_{bar}) f'_c + 1.58A_{bar} f_{y,bar}, \quad (3)$$

$$\alpha_A = 3.8 \left(\frac{A_{bar}}{A_h} \right)^{2/3}, \quad (4)$$

where α_A is the effective shear area ratio of concrete dowel per hole, reflecting the confinement effect of bar on concrete; A_h and A_{bar} are the area of the rib hole and steel bar (mm^2), respectively; f'_c is the concrete cylinder compressive strength (MPa); and $f_{y,bar}$ is the yield strength of the transverse bar (MPa). As shown in Table 3, the shear capacity is calculated to be 204.8 kN, which is smaller than the experimental uplift resistance. The strength is underestimated because the contribution of the chemical bonding effect to shear resistance is ignored in equation (3).

Equation (3) is based on the results of traditional push-out tests. In these tests, steel bars in the rib holes almost failed in shear with limited bending deformation [4]. However, in T-type specimens, the bars have much larger bending deformation. It implies that, as shown in Figure 21, the moment (M_{hs}) in the bar section A is larger in T-type specimens, and thus that the normal stress is larger. Based on the von Mises yield criterion, it is known that the steel bar would yield under smaller shear stress when normal stress is larger. It means the shear resistance of bars in hole in T-type specimens is smaller than that in S-type specimens.

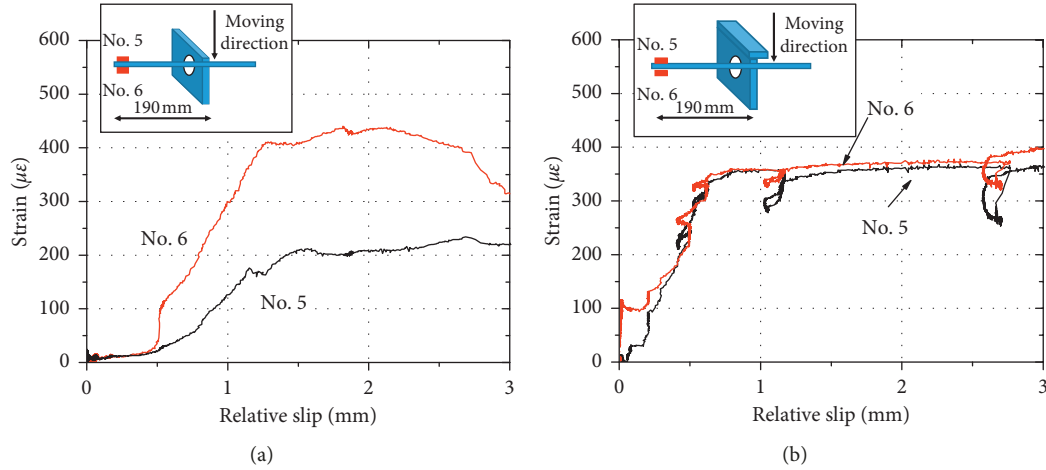


FIGURE 19: Results of no. 5 and no. 6 strain gauges in transverse bars of T-type specimens. (a) T-1. (b) T-2.

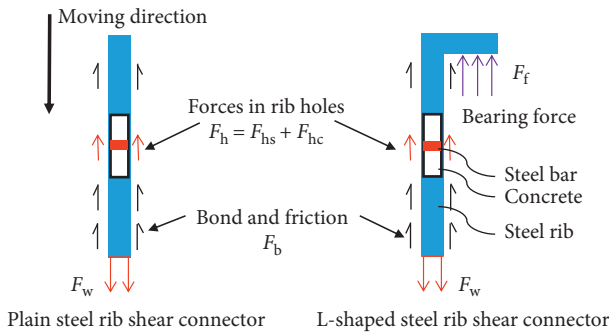


FIGURE 20: Free-body diagram of shear connectors.

TABLE 3: Calculation results of the resistance of concrete dowel and transverse bar.

α_A	A_h ($\times 10^3 \text{ mm}^2$)	A_{bar} ($\times 10^3 \text{ mm}^2$)	f'_c (MPa)	$f_{y,bar}$ (MPa)	$F_{h,u}$ (kN)
0.90	1963.5	153.9	43.0	450.0	204.8

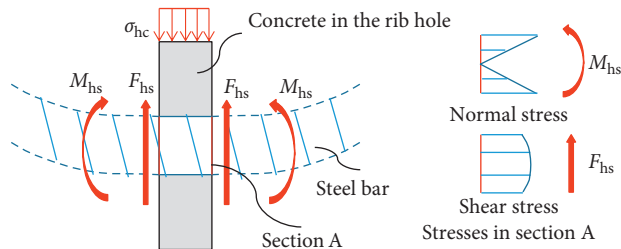


FIGURE 21: Forces and stresses in the transverse steel bar.

3.3. Bond Strength. For steel and concrete composite constructions without shear connectors, natural bonding, friction, and mechanical interlocking actions transfer the stress between steel and concrete members. The stress is referred to as bond stress. The bond stress capacity (τ_u) is reached with the rupture of the chemical adherence between the steel and concrete. Then, the bond stress reduces rapidly

to a value and remains relatively stable after a certain slip. This value is referred to as residual bond stress. Since 1962, many studies [28–30] have addressed the bond stress capacity of steel and concrete composite constructions. The encased steel section compared with the concrete encasement (ρ), the thickness of the concrete cover, and the length of the bond stress region (L_b) was deemed to affect the bond stress capacity [31]. T- and S-type specimens have large differences in the values of ρ and L_b . The bond stress capacity was then estimated through equation (5) by Roeder et al. [31]:

$$\tau_u = 2.91 - 0.300 \left(\frac{L_b}{d} \right) - 14.97\rho, \quad (5)$$

where τ_u is the bond stress capacity (MPa); ρ is the encased steel section compared with the concrete encasement ρ and is equal to (A_s/A_t) ; and d is the depth of steel section (mm). Then, the strength of the bond ($F_{b,u}$) is written as follows:

$$F_{b,u} = \tau_u A_b, \quad (6)$$

where A_b is the contact area between the steel rib and concrete.

The bond fails at a small slip. The ultimate slip at the loaded end of specimens was evaluated according to Yang et al. [32]:

$$S_{bu} = 4.098 \times 10^{-4} I_e. \quad (7)$$

The calculated results are presented in Table 4. The calculated bond stress capacity of S-1 specimen is smaller than those of T-type specimens due to the larger contact area. These results are consistent with experimental ones. The calculated S_{bu} is about 20% of S_u , which indicates that the bond had failed before the specimens reached their ultimate strengths. Therefore, the value of the bond stress at the failure of the specimen was assumed to be equal to the residual bond stress. Only a few studies have been performed to investigate the residual bond stress. In this study, it was taken as 63% of the bond stress capacity according to the test results of 16 push-out specimens by Yang et al. [32]. Then,

TABLE 4: Calculation results of bond strength.

Label	L_b (mm)	d (mm)	ρ (%)	A_b ($\times 10^3$ mm ²)	S_{bu} (mm)	τ_u (MPa)	$F_{b,u}$ (kN)	$F_{b,r}$ (kN)
S-1	400	400	4.8	160	0.20	1.89	302.8	190.8
T-1 and T-2	150	100	1.1	36	0.07	2.29	82.6	52.0

the residual bond strength ($F_{b,r}$) was estimated and is presented in Table 4.

3.4. Contribution of Rib Flange to the Load Capacity. The force at the flange of the rib (F_f) causes a bending moment at the fixed end of the flange. When the force is large enough, a plastic hinge would form. This force is referred to as $F_{frib,u}$. Meanwhile, the equal and opposite forces by the rib flange on the concrete would lead to local crushing or tensile failure of concrete. Thus, the following relationship is obtained:

$$F_{f,u} = \min(F_{frib,u}, F_{fc,u}), \quad (8)$$

where $F_{f,u}$ is the ultimate load at the rib flange and $F_{fc,u}$ is the strength of concrete surrounding the rib flange.

The rib flange embedded in concrete is subjected to complex loading, as shown in Figure 22. The shear force in the left side of the flange is in vertical equilibrium with the reaction forces from concrete. For the rotation equilibrium, moment at the left side of the flange is induced. Here, the concrete bearing stress distribution acting on the rib flange was simply assumed to a triangle in which the width is equal to the width of the rib flange, as shown in Figure 22. Then, the capacity of rib flange ($F_{frib,u}$) can be calculated as follows:

$$F_{frib,u} = \frac{M_{frib,u}}{b_f/3} = \frac{f_{y,rib}(a_{rib}t_{rib}^2/4)}{b_f/3}, \quad (9)$$

where $M_{frib,u}$ is the ultimate sectional bending moment of the rib flange (N-mm) and b_f is the width of the rib flange (mm).

The local bearing strength of concrete under the rib flange was calculated according to the ACI standard [33]:

$$F_{fc,u1} = 8A_{b,0}f'_c = 8a_{rib}b_f f'_c, \quad (10)$$

where $A_{b,0}$ is the net bearing area of the rib flange on the concrete.

After the tension force was transferred by the shear connector to concrete, it induces shear force and bending moment in concrete transverse sections. In Figure 22, section B, which is the weakest concrete section and which passed through the right end of the rib flange, is paid attention to. Section B has a width of 200 mm (a_c) and a height of 100 mm (h_{rib}), and the internal forces in this section consist of a force equal to ($F_{fc,2}/2$) and a moment equal to ($b_f F_{fc,2}/2$). It was assumed that concrete crack occurred when the maximum tensile stress reached the concrete tensile strength. Then, the concrete cracking load is evaluated through the following equation:

$$F_{fc,u2} = 2 \times \frac{M_{fc,u}}{b_f} = 2 \times \frac{f_{ct}(a_c h_{rib}^2/6)}{b_f}, \quad (11)$$

where a_c is the width of section B, h_{rib} is the rib height, and $M_{fc,u}$ is the ultimate sectional bending moment of section B. The calculated results are presented in Table 5.

3.5. Punching Strength of Concrete. The shear connector exerts on the remaining concrete and steel bar forces equal and opposite to the forces exerted by the remaining concrete and steel bar on the shear connector. The forces in the concrete lead to punching shear failure. Concrete cone would be punched out, and its geometry shows the mechanical characteristics of the shear connector and was reported to be influenced by steel bar diameter [24]. Concrete cones developed on both sides of the shear connectors in the T-type specimens, as shown in Figure 23. The geometry of the concrete cones was carefully measured and is presented in Table 6 with the aim to estimate the load when the concrete failure prism forms. The height of the cones is about half of the height of the steel rib, while the inclination of the shear cracks ranges from 11.1° to 22.3°. The strength was estimated by referring to the calculation method for the punching shear strength of concrete slab. Steel reinforcements were not arranged in the concrete cones. Therefore, the concrete cones were assumed to form when the tensile stress of concrete along the cone surface reached its tensile strength. Then, equation (12) is derived as

$$F_{c,u} = f_{ct}A_p = f_{ct}B_p(L_{p,left} + L_{p,right}), \quad (12)$$

where A_p is the projected area of concrete cone, B_p is the width of concrete cone, L_p is the length of the concrete cone, and θ_1 is the concrete cone angle.

4. Discussions

The calculated results are summarized in Table 7. The failure modes of the specimens are discussed by the comparison between the calculated and experimental results.

S-1 specimen which failed in ductile mode of failure is a traditional push-out test specimen. Its failure mode is similar to that reported in [12]. Its shear capacity can be written as the sum of the strength of the concrete dowel and transverse steel bar in the hole and the residual bond strength, as shown in equation (13). The ratio of the predicted strength to the tested one is 1.09, which shows a good level of accuracy of the predict method.

$$F_u = F_{h,u} + F_{b,r}. \quad (13)$$

T-1 specimen failed in brittle mode of failure. The estimated $F_{c,u}$ for T-1 specimen is close to the experimental

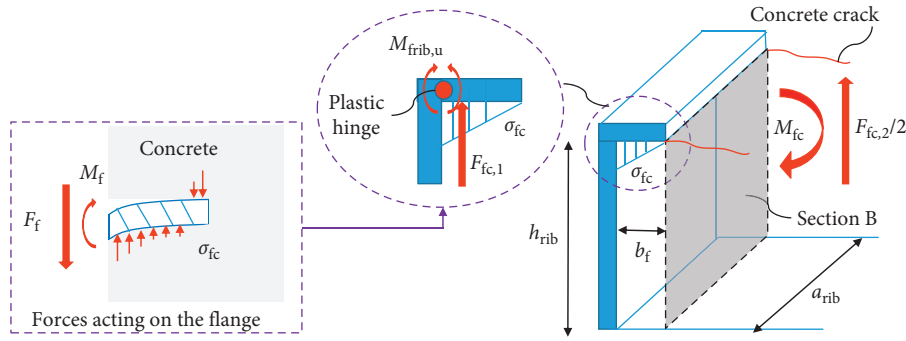


FIGURE 22: Force diagram of L-shaped steel rib shear connector.

TABLE 5: Calculation results of the contribution of rib flange to the load capacity.

Label	b_f (mm)	a_{rib} (mm)	a_c (mm)	t_{rib} (mm)	h_{rib} (mm)	$f_{y,rib}$ (MPa)	f'_c (MPa)	f_{ct} (MPa)	$A_{b,0}$ ($\times 10^3$ mm ²)	$F_{rib,u}$ (kN)	$F_{fc,u1}$ (kN)	$F_{fc,u2}$ (kN)	$F_{f,u}$ (kN)
T-2	30	180	200	6	100	365	43.0	4.6	6	59.1	1857.6	102.2	59.1

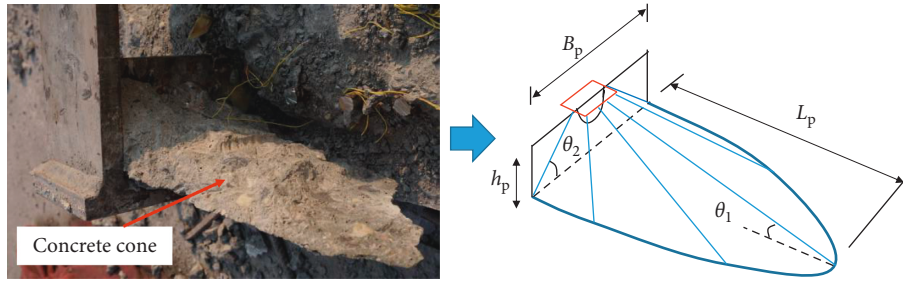


FIGURE 23: Concrete cone in T-type specimen.

TABLE 6: Calculation results of the punching strength of concrete.

Label	f_{ct} (MPa)	B_p (mm)	$L_{p,left}$ (mm)	$L_{p,right}$ (mm)	$\theta_{1,left}$ (deg)	$\theta_{1,right}$ (deg)	A_p ($\times 10^4$ mm ²)	$F_{c,u}$ (kN)
T-1	4.6	200	160.1	255.0	17.3	11.1	8.3	381.9
T-2	4.6	200	121.7	180.3	22.3	15.5	6.0	277.8

TABLE 7: Summary of calculated results.

Label	F_u (kN)	$F_{w,u}$ (kN)	$F_{h,u}$ (kN)	$F_{b,u}$ (kN)	$F_{b,r}$ (kN)	$F_{c,u}$ (kN)	$F_{rib,u}$ (kN)	$F_{fc,u1}$ (kN)	$F_{fc,u2}$ (kN)	$F_{f,u}$ (kN)	$F_{h,u} + F_{b,r}$ (kN)	$F_{u,CAL}$ (kN)	$F_{u,CAL}/F_u$
S-1	363.3	—	204.8	302.8	190.8	—	—	—	—	—	395.6	395.6	1.09
T-1	367.8	394.2	204.8	82.6	52.0	381.9	—	—	—	—	256.8	381.9	1.04
T-2	328.5	394.2	204.8	82.6	52.0	277.8	59.1	1857.6	102.2	59.1	256.8	336.9	1.03

ultimate strength. It seems that the punching shear failure of concrete triggered the failure of the specimen, though the calculated ($F_{h,u} + F_{b,r}$) is smaller than $F_{c,u}$. Considering that equation (13) for traditional push-out test specimen might not apply to T-type specimen, the capacity of T-1 specimen was calculated through equation (14). It can be seen that the predicted method is good.

$$F_u = F_{c,u} \quad (14)$$

T-2 specimen also failed in brittle mode of failure. $F_{c,u}$ for T-2 specimen is about 72.7% of that for T-1 specimen. In T-2 specimen, $F_{c,u}$ was thought to be affected by the horizontal crack initiated near the rib flange. $F_{fc,u1}$ and

$F_{fc,u2}$ are larger than $F_{rib,u}$, which implies that when the plastic hinge formed, the concrete under the rib flange would not crush or crack. The contribution of the rib flange to the uplift resistance $F_{f,u}$ was equal to $F_{rib,u}$ and remained constant after the plastic hinge formed. The capacity of T-2 specimen was calculated through equation (15). As shown in Table 7, a good level of accuracy of the predict method was obtained.

$$F_u = F_{c,u} + F_{f,u} \quad (15)$$

In summary, there are three potential failure modes of the perforated rib shear connector under uplift forces, as shown in Figure 24. One is the yielding of the steel rib web.

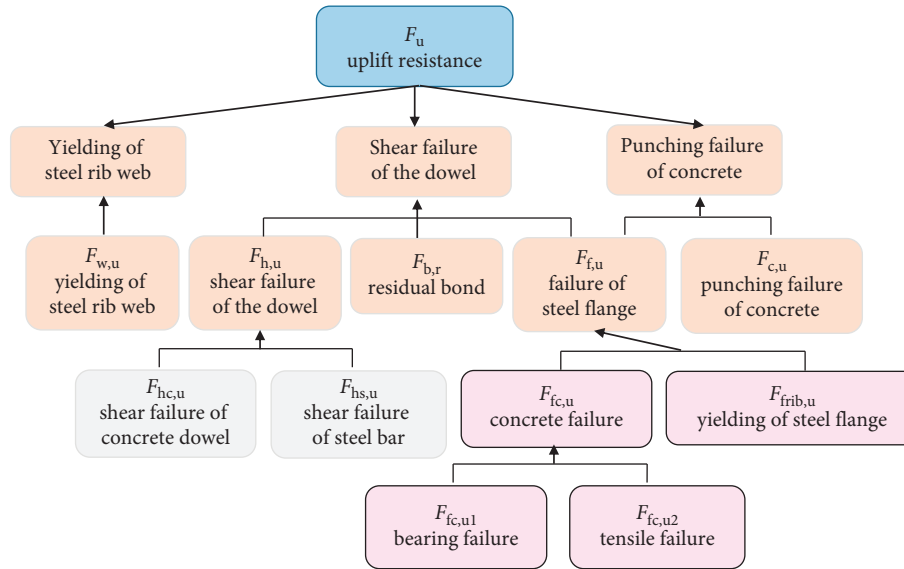


FIGURE 24: Scheme of failure mechanisms of perforated rib shear connectors under uplift forces.

The second one is the shear failure of the concrete dowel and transverse steel bar in the hole, which is a ductile failure mode and is similar to that when the shear connector is under shear forces. The last one is the punching shear failure of concrete under the steel rib, which is a brittle failure mode. The uplift resistance of the shear connector is the smallest failure capacity of these three failure modes, as given in the following equation:

$$F_u = \min(F_{w,u}, F_{h,u} + F_{b,r} + F_{f,u}, F_{c,u} + F_{f,u}). \quad (16)$$

In this study, the horizontal crack at the height of the rib flange has a significant unfavorable effect on the uplift resistance of the L-shaped rib shear connector. Thus, a proper design of the rib flange is required to avoid premature cracks in concrete, and the rib flange should be designed to meet the following inequality equation (17). According to equation (11), $F_{fc,u2}$ is in proportion to the height of the rib and inversely proportional to the width of the rib flange. Considering that the bond strength and the concrete punching shear strength also increase with the height of the rib, increasing the rib height is recommended to avoid the horizontal crack.

$$F_u \leq F_{fc,u2}. \quad (17)$$

5. Conclusions

This paper presented the test results of 3 push-out specimens for perforated steel rib shear connectors. Two of them were designed to reflect the real state of perforated steel rib shear connectors in steel and concrete composite slabs with the aim of investigating the uplift behavior of the connectors. The failure modes of the rib shear connectors are analyzed, and analytical models for the determination of the uplift resistance are derived based on test results. The following conclusions can be drawn:

- (1) Since the thickness of concrete block to support the steel bar in the hole of the perforated rib is small, the failure mode of the specimens under uplift force is different from that under shear force. The concrete below the bar was pushed out, and the transverse steel bars had much larger bending deformation. Though the ultimate strength of perforated rib in composite slab under uplift force was close to that under shear force, the ductility and residual capacity were smaller.
- (2) When the L-shaped perforated rib was under uplift force, cracks would develop at the height of the short leg of the L-shaped rib and propagate horizontally. As a result, the L-shaped rib shear connector had an ultimate strength 10.7% smaller than that of the plain rib shear connector.
- (3) The punching shear failure of concrete triggered the failure of the plain rib shear connector. For the L-shaped rib shear connector, a plastic hinge would form at the end of the rib flange. The contribution of the rib flange to the uplift resistance would remain constant after the plastic hinge formed and should be taken into consideration.
- (4) The validity of the analytical models was confirmed by comparing the failure modes and load capacities of specimens. It was suggested to increase the rib height of the L-shaped rib to avoid the horizontal crack at the height of the rib flange.

Our study contributes to the understanding of the behavior of perforated steel rib shear connectors. The proposed equations for the uplift resistance of the connector are beneficial to the design and maintenance of composite structures. The experimental results of this paper represent a relatively small database. In the future, additional experimental and theoretical studies will be conducted to validate the proposed models.

Notations

a_c :	Width of the weakest concrete transverse section
a_{rib} :	Width of the web of steel rib
A_b :	Contact area between the steel rib and concrete
A_{bar} :	Area of the steel bar
$A_{b,0}$:	Net bearing area of the rib flange on the concrete
A_h :	Area of the steel rib hole
A_p :	Projected area of the concrete cone
A_s :	Area of the encased steel section
A_t :	Area of total cross section of the specimen
A_w :	Cross-sectional area of the web of steel rib
b_f :	Width of the flange of the L-shaped rib
B_p :	Width of concrete cone
d :	Depth of steel section
d_h :	Diameter of the rib hole
d_s :	Diameter of the transverse bar
E_c :	Elastic modulus of concrete
f'_c :	Concrete cylinder compressive strength
f_{ct} :	Concrete tensile strength
f_{cu} :	Concrete cube compressive strength
$f_{y,bar}$:	Yield strength of the transverse bar
$f_{y,rib}$:	Yield strength of the steel rib
F_b :	Bond and friction
$F_{b,r}$:	Residual bond strength
$F_{b,u}$:	Ultimate bond strength
F_f :	Force applied on the flange of the L-shaped rib
$F_{fc,1}$:	Local bearing force of concrete under the flange of the L-shaped rib
$F_{fc,2}$:	Shear force in the weakest concrete transverse section
$F_{fc,u}$:	Strength of concrete under the flange of the L-shaped rib
$F_{fc,u,1}$:	Local bearing strength of concrete under the flange of the L-shaped rib
$F_{fc,u,2}$:	Cracking strength of concrete under the flange of the L-shaped rib
$F_{frib,u}$:	Load of the plastic hinge forming in the flange of the L-shaped rib
$F_{f,u}$:	Maximum value of F_f
F_{hc} :	Shear force in the concrete dowel
F_{hs} :	Shear force in the transverse bar
F_r :	Residual load capacity
F_w :	Tensile force in the rib web
$F_{w,u}$:	Maximum value of F_w
F_u :	Ultimate load
$F_{u,CAL}$:	Calculated load capacity
h_{rib} :	Rib height
L_b :	Length of steel section or bond stress interface length
L_p :	Length of concrete cone
$M_{f,u}$:	Ultimate sectional bending moment of the flange of the L-shaped rib
$M_{fc,u}$:	Ultimate sectional bending moment of the weakest concrete transverse section
M_{hs} :	Moment in the transverse bar
P_u :	Estimated ultimate load
S_{bu} :	Ultimate slip when the bond fails
S_u :	Ultimate slip when the specimen fails

t_{rib} :	Thickness of the steel rib
W_{fc} :	Proportional limit force
α_A :	Effective shear area ratio of concrete dowel per hole
θ_1 :	Concrete cone angle
ρ :	A_t/A_c
σ_{fc} :	Compressive stress on the rib flange
τ_u :	Bond stress capacity.

Data Availability

All data included in this study are available from the corresponding author upon request.

Conflicts of Interest

The authors declare that there are no conflicts of interest regarding the publication of this paper.

Acknowledgments

This work was supported by the National Natural Science Foundation of China (grant no. 51808069), the National Key Research and Development Program of China (grant no. 2016YFC0701202), and the Fundamental Research Funds for the Central Universities (grant no. 2018CDXYTM0003).

References

- [1] D. J. Oehlers and M. A. Bradford, *Elementary Behaviour of Composite Steel and Concrete Structural Members*, Butterworth-Heinemann, Oxford, UK, 1999.
- [2] F. Leonhardt, W. Andrä, H.-P. Andrä, and W. Harre, "Neues, vorteilhaftes verbundmittel für stahlverbund-tragwerke mit hoher dauerfestigkeit," *Beton-und Stahlbetonbau*, vol. 82, no. 12, pp. 325–331, 1987.
- [3] V. Isabel and J. S. C. Paulo, "Experimental analysis of perfobond shear connection between steel and lightweight concrete," *Journal of Constructional Steel Research*, vol. 60, no. 3–5, pp. 465–479, 2004.
- [4] S. Zheng, Y. Liu, T. Yoda, and W. Lin, "Parametric study on shear capacity of circular-hole and long-hole perfobond shear connector," *Journal of Constructional Steel Research*, vol. 117, pp. 64–80, 2016.
- [5] X. Xu, Y. Liu, and Y. Zuo, "Contribution of perforated steel ribs to load-carrying capacities of steel and concrete composite slabs under negative bending," *Advances in Structural Engineering*, vol. 21, no. 12, pp. 1879–1894, 2018.
- [6] H.-Y. Kim, Y.-J. Jeong, T.-H. Kim, and S.-K. Park, "Structural performance of steel-concrete composite deck for steel-box girder bridges," *KSCE Journal of Civil Engineering*, vol. 10, no. 5, pp. 357–363, 2006.
- [7] C. H. Chung, J. Lee, and J. S. Kim, "Shear strength of T-type perfobond rib shear connectors," *KSCE Journal of Civil Engineering*, vol. 20, no. 5, pp. 1824–1834, 2016.
- [8] X. Liu, C. Xu, J. Liu, and Y. Yang, "Research on special-shaped concrete-filled steel tubular columns under axial compression," *Journal of Constructional Steel Research*, vol. 147, pp. 203–223, 2018.
- [9] Y. Liu, H. Xin, and Y. Liu, "Load transfer mechanism and fatigue performance evaluation of suspender-girder composite anchorage joints at serviceability stage," *Journal of Constructional Steel Research*, vol. 145, pp. 82–96, 2018.

- [10] E. C. Oguejiofor and M. U. Hosain, "A parametric study of perfobond rib shear connectors," *Canadian Journal of Civil Engineering*, vol. 21, no. 4, pp. 614–625, 1994.
- [11] J.-H. Ahn, C.-G. Lee, J.-H. Won, and S.-H. Kim, "Shear resistance of the perfobond-rib shear connector depending on concrete strength and rib arrangement," *Journal of Constructional Steel Research*, vol. 66, no. 10, pp. 1295–1307, 2010.
- [12] C. Zhao, Z. Li, K. Deng, and W. Wang, "Experimental investigation on the bearing mechanism of perfobond rib shear connectors," *Engineering Structures*, vol. 159, pp. 172–184, 2018.
- [13] W. Lorenc, M. Kożuch, and S. Rowiński, "The behaviour of puzzle-shaped composite dowels—part II: theoretical investigations," *Journal of Constructional Steel Research*, vol. 101, pp. 500–518, 2014.
- [14] M. Kopp, K. Wolters, M. Classen et al., "Composite dowels as shear connectors for composite beams—background to the design concept for static loading," *Journal of Constructional Steel Research*, vol. 147, pp. 488–503, 2018.
- [15] M. Classen and J. Hegger, "Shear-slip behaviour and ductility of composite dowel connectors with pry-out failure," *Engineering Structures*, vol. 150, pp. 428–437, 2017.
- [16] M. Classen and J. Hegger, "Assessing the pry-out resistance of open rib shear connectors in cracked concrete—engineering model with aggregate interlock," *Engineering Structures*, vol. 148, pp. 254–262, 2017.
- [17] M. Classen and J. Hegger, "Shear tests on composite dowel rib connectors in cracked concrete," *ACI Structural Journal*, vol. 115, no. 3, pp. 661–671, 2018.
- [18] M. Classen and J. Gallwoszus, "Concrete fatigue in composite dowels," *ACI Structural Concrete*, vol. 17, no. 1, pp. 63–73, 2016.
- [19] S.-H. Kim, J.-H. Yoon, J.-H. Kim, W.-J. Choi, and J.-H. Ahn, "Structural details of steel girder-abutment joints in integral bridges: an experimental study," *Journal of Constructional Steel Research*, vol. 70, pp. 190–212, 2012.
- [20] Y. Liu, Z. Xiong, Y. Feng et al., "Concrete-filled rectangular hollow section X joint with perfobond leister rib structural performance study: ultimate and fatigue experimental investigation," *Steel and Composite Structures*, vol. 24, no. 4, pp. 455–465, 2017.
- [21] European Committee for Standardization, *EN 1994-1-1:2004, Eurocode 4: Design of Composite Steel and Concrete Structures—Part 1-1: General Rules and Rules for Buildings*, European Committee for Standardisation, Brussels, Belgium, 2004.
- [22] M. Classen and J. Hegger, "Anchorage of composite dowels," *Steel Construction*, vol. 9, no. 2, pp. 138–150, 2016.
- [23] M. Classen, J. Gallwoszus, and A. Stark, "Anchorage of composite dowels in UHPC under fatigue loading," *Structural Concrete*, vol. 17, no. 2, pp. 183–193, 2016.
- [24] M. Classen, J. Bielak, and D. Huerth, "Rib shear connectors with concrete break out failure subjected to tension or compressive loads—part 1: finite element analysis," *Beton-und Stahlbetonbau*, vol. 113, no. 5, pp. 348–359, 2018.
- [25] M. Classen, P. Schmidt, and D. Huerth, "Rib shear connectors with concrete break out failure subjected to tension or compressive loads—part 2: database and design models," *Beton-und Stahlbetonbau*, vol. 113, no. 6, pp. 443–452, 2018.
- [26] M. Classen, M. Herbrand, V. Adam, D. Kueres, and M. Sarac, "Puzzle-shaped rib shear connectors subjected to combined shear and tension," *Journal of Constructional Steel Research*, vol. 145, pp. 232–243, 2018.
- [27] M. Classen, V. Adam, D. Kueres et al., "Pull-out and shear interaction of puzzle-shaped composite dowels," *Beton-und Stahlbetonbau*, vol. 112, no. 6, pp. 334–345, 2017.
- [28] J. O. Brynson and R. G. Mathey, "Surface condition effect on bond strength of steel beams embedded in concrete," *Journal of ACI*, vol. 59, no. 3, pp. 397–405, 1962.
- [29] Y. J. Jeong, H. Y. Kim, H. B. Koo, and S. T. Kim, "Steel-concrete interface behavior and analysis for push-out," *KSCE Journal of Civil Engineering*, vol. 9, no. 2, pp. 119–124, 2005.
- [30] L. Chen, J. Dai, Q. Jin, L. Chen, and X. Liu, "Refining bond-slip constitutive relationship between checkered steel tube and concrete," *Construction and Building Materials*, vol. 79, pp. 153–164, 2015.
- [31] C. W. Roeder, R. Chmielowski, and C. B. Brown, "Shear connector requirements for embedded steel sections," *Journal of Structural Engineering*, vol. 125, no. 2, pp. 142–151, 1999.
- [32] Y. Yang, Z. Guo, J. Xue et al., "Experiment study on bond slip behavior between section steel and concrete in SRC structures," *Journal of Building Structures*, vol. 26, no. 4, pp. 1–9, 2005, in Chinese.
- [33] American Concrete Institute, *ACI 318M: Building Code Requirements for Structural Concrete (ACI 318M-11) and Commentary*, American Concrete Institute, Farmington Hills, MI, USA, 2011.

